Journal of Zhejiang University-SCIENCE A 2026 27(3):306-316
www.jzus.zju.edu.cn; www.springer.com/journal/11582
E-mail: jzus_a@zju.edu.cn

Research Article
https://doi.org/10.1631/jzus.A2500350

A heterogeneous cyclic Hopfield neural network without self-connections

Yunzhen ZHANG[1], Chunlong ZHOU[1,2], Han BAO[2]✉, Guangzhe ZHAO[1], Bocheng BAO[2]

[1]*School of Information Engineering, Xuchang University, Xuchang 461000, China*
[2]*Wang Zheng School of Microelectronics, Changzhou University, Changzhou 213159, China*

Abstract: We propose a three-neuron heterogeneous cyclic Hopfield neural network (het-CHNN) utilizing three different activation functions: the hyperbolic tangent, sine, and cosine functions. The network's globally uniformly ultimate boundedness is proved theoretically, and its chaotic dynamics are explored through numerical simulations and analog experiments. The numerical results demonstrate that the het-CHNN displays chaotic dynamics and multi-scroll chaotic attractors. Subsequently, the het-CHNN is implemented in an analog circuit, and hardware experiments are performed to verify the previous numerical results. Notably, the het-CHNN successfully resolves the issue of the absence of chaos in a three-neuron CHNN and currently appears to be the simplest three-neuron Hopfield neural network (HNN) that can generate chaos.

Key words: Activation function; Analog circuit; Chaos; Cyclic Hopfield neural network (CHNN); Multi-scroll chaotic attractor

1 Introduction

Hopfield neural networks (HNNs) have attracted considerable research attention due to their unique network framework and their ability to produce complex dynamics similar to those in the brain (Hopfield, 1982). HNNs are regarded as a specific type of dynamical system (Lin et al., 2022). Similar to most dynamical systems, HNNs exhibit complex dynamics due to their inherent activation functions (Rech, 2015). Recently, many improved versions of HNNs have been proposed, such as the memristive bi-neuron HNN (Li et al., 2024b), conventional three-dimensional (3D) HNN (Bao et al., 2019; Njitacke et al., 2021), magnetized HNN (Wan et al., 2023), memristor-driven HNN (Lai et al., 2023; Lin et al., 2023; Yu et al., 2023), two-memristor-driven HNN (Bao H et al., 2024; Li et al., 2025), locally active memristive HNN (Tang et al., 2024), dual-neuron memristive HNN (Liu et al., 2025), fractional-order HNN (Xu et al., 2022), and diagonal rotor HNN (Kobayashi, 2020). These improved models have furthered the understanding of the intrinsic dynamics of HNNs (Danca and Kuznetsov, 2017) and are beneficial for many HNN-based industrial applications (Bao BC et al., 2024; Lai et al., 2024; Yu et al., 2025a, 2025b).

In the aforementioned studies, the hyperbolic tangent function is generally used as the activation function for the neurons in HNNs; moreover, the same activation function is used for each neuron, indicating that the neurons are homogenous. However, it is widely believed that the brain contains a broad variety of complex neurons, reflecting its sophisticated nature (Zhang et al., 2021; Prescott and Liberles, 2022). Such characteristics of neural network dynamics have been studied for various types of neurons (Chen et al., 2024). Furthermore, the heterogeneity of HNNs is considered theoretically similar to the pathogenesis of some neurological disorders (such as Parkinson's disease) (Gratwicke et al., 2015). Therefore, the study of heterogeneous HNNs with varying neuron types holds great practical significance in the field of biology. However, research on heterogeneous activation functions in HNNs has not received sufficient attention, with relatively few published studies available (Wang et al., 2024).

✉ Han BAO, hanbao@cczu.edu.cn
Yunzhen ZHANG, https://orcid.org/0000-0002-1433-0487
Han BAO, https://orcid.org/0000-0002-2329-6890

Received July 26, 2025; Revision accepted Sept. 12, 2025;
Crosschecked Jan. 4, 2026; Online first Feb. 4, 2026

The unidirectional cyclic HNN (CHNN) has a relatively simple connection structure. In the neurons of an HNN, the unidirectional connection weights with a gradient distribution of energy dominate, and through adaptive connection weights, energy balance and phase locking can be easily achieved (Xie et al., 2022; Ma, 2023; Lei et al., 2025). Unfortunately, it has been demonstrated that the three-neuron CHNN fails to present chaotic dynamics (Yang, 2008). To address this issue, a four-dimensional memristive three-neuron CHNN based on changeable connection weights was constructed to exhibit chaotic and coexistence behaviors (Bao et al., 2022). In this study, we expand upon these works and propose a novel 3D heterogeneous CHNN (3D het-CHNN) with three neurons and without self-connections, which employs three different activation functions. Due to the plasticity of neurons (McFarlan et al., 2023), connections between neurons may be disrupted in certain diseases, such as epilepsy, schizophrenia, and Alzheimer's disease (Korn and Faure, 2003), resulting in the absence of self-connections; thus, our proposed network emulates this biological phenomenon. Although the network is unidirectional and has no self-connections, it is capable of generating strange multi-scroll chaotic attractors. We demonstrate that the 3D het-CHNN is a highly simple three-neuron HNN that can generate chaos. Studying the dynamical behavior of this novel HNN architecture therefore has both theoretical and practical significance.

Furthermore, compared with single-scroll attractors, multi-scroll chaotic attractors have more complex motion trajectories and topological structures, with their trajectories being able to randomly jump between multiple different attractor scrolls (Lai et al., 2024; Tang et al., 2024). Neuronal firing behavior in the brain exhibits similar complexity and diversity in terms of trajectories and attractors. Therefore, the multi-scroll chaotic attractor discovered in the proposed 3D het-CHNN reflects the complexity of brain dynamics.

The rest of this study is organized as follows. Section 2 presents the architecture of the 3D het-CHNN and investigates its boundedness and equilibrium point stability. Section 3 explores its bifurcation dynamics, multi-scroll chaotic attractor, and bi-stability through numerical simulations. In Section 4, the 3D het-CHNN is implemented with an analog circuit to validate the numerical results. Finally, Section 5 summarizes the findings.

2 Heterogeneous CHNN with three neurons

In this section, we propose a novel 3D het-CHNN with three different types of activated neurons. Based on its mathematical model, the boundedness and equilibrium point stability are investigated for the 3D het-CHNN.

2.1 Model descriptions

HNNs have been widely studied due to their unique framework and their ability to produce complex dynamics similar to those in the brain. The 3D het-CHNN with three neurons is described by:

$$\dot{\boldsymbol{x}}=-\boldsymbol{x}+\boldsymbol{G}\boldsymbol{f}(\boldsymbol{x}), \tag{1}$$

where $\boldsymbol{x}=[x_1, x_2, x_3]^{\mathrm{T}}\in\mathbb{R}^3$ is the membrane potential vector, $\boldsymbol{G}=[g_{ij}]\in\mathbb{R}^{3\times3}$ is the synaptic weight matrix, and $\boldsymbol{f}(\boldsymbol{x})=[f_1(x_1), f_2(x_2), f_3(x_3)]^{\mathrm{T}}\in\mathbb{R}^3$ is the activation function vector.

The 3D het-CHNN framework is illustrated in Fig. 1. It is a 3D ordinary differential dynamical system composed of three neurons that are unidirectionally and cyclically connected. Three activation functions—the hyperbolic tangent, sine, and cosine nonlinearities—were used as the activation functions of the neurons. Hence, the activation function vector is described as:

$$\boldsymbol{f}(\boldsymbol{x})=[\tanh x_1,\ \sin x_2,\ \cos x_3]^{\mathrm{T}}. \tag{2}$$

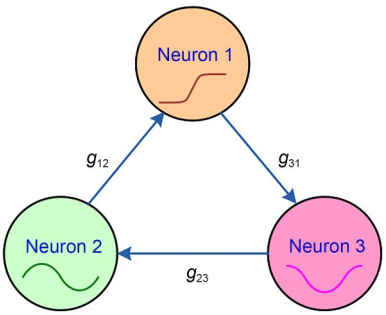

Fig. 1 Framework of the three-neuron het-CHNN without self-connections

These three diverse activation functions enable the HNN to achieve heterogeneous connections.

Notably, the hyperbolic tangent function exhibits monotonic nonlinear characteristics, while the sine and cosine functions both have non-monotonic nonlinear characteristics. The literature (Lin and Chen, 2009) has

reported that using non-monotonic activation functions in neural networks can enhance their memory capabilities, and due to the resulting expansion in the number of equilibrium points, diverse chaotic dynamics are more likely to be triggered. These advantages have been confirmed in neural networks that incorporate sine or cosine activation functions (Chen et al., 2021; Zhou et al., 2026).

In Fig. 1, one can see that none of the three neurons have self-connections, so elements g_{11}, g_{22}, and g_{33} do not appear in the synaptic weight matrix, i.e., g_{11}=0, g_{22}=0, and g_{33}=0. Furthermore, since the three neurons are connected in a unidirectional, clockwise, and circular manner, the elements g_{13}, g_{21}, and g_{32} do not exist in the synaptic weight matrix, i.e., g_{13}=0, g_{21}=0, and g_{32}=0. Therefore, according to the framework, the synaptic weight matrix can be written as:

$$\boldsymbol{G}=\begin{bmatrix} g_{11} & g_{12} & g_{13} \\ g_{21} & g_{22} & g_{23} \\ g_{31} & g_{32} & g_{33} \end{bmatrix}=\begin{bmatrix} 0 & g_{12} & 0 \\ 0 & 0 & g_{23} \\ g_{31} & 0 & 0 \end{bmatrix}. \tag{3}$$

By combining the expressions in Eqs. (1)–(3), the mathematical model of the 3D het-CHNN can be rewritten in a concise form as:

$$\begin{cases} \dot{x}_1=-x_1+g_{12}\sin x_2, \\ \dot{x}_2=-x_2+g_{23}\cos x_3, \\ \dot{x}_3=-x_3+g_{31}\tanh x_1. \end{cases} \tag{4}$$

This indicates that the 3D het-CHNN is a simple dynamical system with three nonlinear coupling terms. In particular, the 3D het-CHNN is the simplest three-neuron HNN that can present chaotic dynamics, thus successfully resolving the issue of the absence of chaos in a three-neuron CHNN.

We set the synaptic weights as g_{12}=4.2, g_{23}=12.0, and g_{31}=−8.6 and determine the initial states as IS=[x_1(0), x_2(0), x_3(0)]=(0.001, 0, 0). The fourth-order Runge-Kutta (RK-4) method with a step size of 0.01 is used for the numerical simulations in MATLAB, with Wolf's Jacobi algorithm with a step size of 1 and a time end of 15000 used for calculating the Lyapunov exponents (LEs) (λ_1, λ_2, λ_3). The 3D het-CHNN can produce a multi-scroll chaotic attractor with (λ_1, λ_2, λ_3)=(0.2380, −0.0001, −3.2679), and its phase orbits in the x_1-x_2 and x_2-x_3 planes are drawn in Fig. 2. Interestingly, the generated chaotic attractor presents a complex multi-scroll geometric structure.

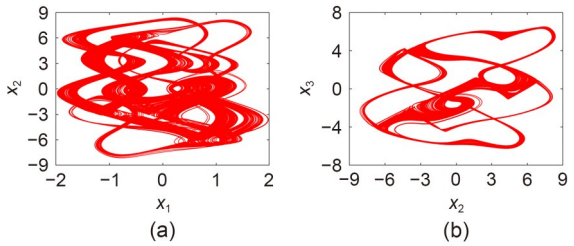

Fig. 2 Phase orbits of the multi-scroll chaotic attractor in the (a) x_1–x_2 plane and (b) x_2–x_3 plane for g_{12}=4.2, g_{23}=12.0, g_{31}=−8.6, and IS=(0.001, 0, 0)

2.2 Proof of boundedness

Consider a nonlinear dynamical system given by:

$$\dot{\boldsymbol{x}}=h(t,\boldsymbol{x}), \tag{5}$$

where h: $\mathbb{R}_+\times D\to\mathbb{R}^n$ is piecewise continuous in time t and is locally Lipschitz in $\boldsymbol{x}$ on $\mathbb{R}_+\times D$, and $D\subset\mathbb{R}^n$ is a domain that contains the origin. To demonstrate the uniform boundedness and ultimate boundedness of the system in Eq. (5), we use the following definition.

Definition 1 (Khalil, 2002, Definition 4.6) The solutions of Eq. (5) are:

(1) uniformly bounded if there exists a positive constant c, independent of $t_0\geqslant 0$, and for every $a\in(0, c)$, $\beta=\beta(a)>0$, independent of t_0, such that

$$\|\boldsymbol{x}(t_0)\|\leqslant a\Rightarrow\|x(t)\|\leqslant\beta,\ \forall t\geqslant t_0;$$

(2) globally uniformly bounded if Eq. (5) holds for arbitrarily large a;

(3) uniformly ultimately bounded with ultimate bound b if there exist positive constants b and c, independent of $t_0\geqslant 0$, and for every $a\in(0, c)$, there is $T=T(a, b)\geqslant 0$, independent of t_0, such that

$$\|\boldsymbol{x}(t_0)\|\leqslant a\Rightarrow\|\boldsymbol{x}(t)\|\leqslant b,\ \forall t\geqslant t_0+T;$$

(4) globally uniformly ultimately bounded if Eq. (5) holds for arbitrarily large a.

With the mathematical model in Eq. (4), we can prove that both the periodic orbits and chaotic orbits of the het-CHNN are confined within a congruous bounded region.

Since the absolute values of the derivatives of the three nonlinear terms in the 3D het-CHNN described by Eq. (4) are all less than or equal to 1, the 3D het-CHNN

is globally Lipschitz continuous. Furthermore, the piecewise continuity of the 3D het-CHNN with respect to time t is a naturally established and self-evident property. Here, we present the proof of the globally uniformly ultimate boundedness of the 3D het-CHNN.

In reference to Li et al. (2024a), a Lyapunov function is constructed as:

$$V(\boldsymbol{x}) = V(x_1, x_2, x_3) = 0.5(x_1^2 + x_2^2 + x_3^2), \quad (6)$$

where $V(\boldsymbol{x})$ is positive definite for $\boldsymbol{x} \in \mathbb{R}^3$ and is radially unbounded. The derivative of Eq. (6) is obtained as:

$$\dot{V}(\boldsymbol{x}) = x_1\dot{x}_1 + x_2\dot{x}_2 + x_3\dot{x}_3 = -x_1^2 - x_2^2 - x_3^2 + v(\boldsymbol{x}), \quad (7)$$

where

$$v(\boldsymbol{x}) = g_{12}x_1 \sin x_2 + g_{23}x_2 \cos x_3 + g_{31}x_3 \tanh x_1. \quad (8)$$

Since $|\sin x_2| \leqslant 1$, $|\cos x_3| \leqslant 1$, and $|\tanh x_1| < 1$, we can obtain the following by using the inequality $|pq| \leqslant 0.5p^2 + 0.5q^2$:

$$\begin{cases} |g_{12}x_1 \sin x_2| \leqslant 0.5g_{12}^2 + 0.5x_1^2, \\ |g_{23}x_2 \cos x_3| \leqslant 0.5g_{23}^2 + 0.5x_2^2, \\ |g_{31}x_3 \tanh x_1| < 0.5g_{31}^2 + 0.5x_3^2. \end{cases} \quad (9)$$

Substituting Eqs. (8) and (9) into Eq. (7) yields:

$$\dot{V}(\boldsymbol{x}) < -0.5(x_1^2 + x_2^2 + x_3^2) + 0.5(g_{12}^2 + g_{23}^2 + g_{31}^2). \quad (10)$$

According to the boundedness theorem of Khalil (2002), let $\mu > 0$, and when $\|\boldsymbol{x}\| \geq \mu$, we have:

$$\dot{V}(\boldsymbol{x}) < -0.5\|\boldsymbol{x}\|^2 + 0.5G^2, \quad (11)$$

where $G = \sqrt{g_{12}^2 + g_{23}^2 + g_{31}^2}$.

Next, we select $\theta \in (0, 1)$ and split the above inequality of Eq. (11) into:

$$\dot{V}(\boldsymbol{x}) < -0.5(1-\theta)\|\boldsymbol{x}\|^2 - 0.5\theta\|\boldsymbol{x}\|^2 + 0.5G^2. \quad (12)$$

Then,

$$\dot{V}(\boldsymbol{x}) < -0.5(1-\theta)\|\boldsymbol{x}\|^2, \ \forall \|\boldsymbol{x}\| \geqslant \mu = \frac{G}{\sqrt{\theta}}. \quad (13)$$

This indicates that when $\|\boldsymbol{x}\| \geqslant \mu$, the derivative satisfies the negative definite condition. We conclude that the solutions are globally uniformly ultimately bounded.

An extra step can be performed to calculate the ultimate bound. In this case, the upper bound α_1 and lower bound α_2 of the Lyapunov function are obtained as $\alpha_1(r) = 0.5r^2$ and $\alpha_2(r) = 0.5r^2$, where r is a positive constant. Thus, according to Theorem 4.18 of Khalil (2002), the ultimate bound can be determined as:

$$b = \alpha_1^{-1}(\alpha_2(\mu)) = \sqrt{\frac{\alpha_2(\mu)}{\alpha_1(1)}} = \sqrt{\frac{0.5\left(\frac{G}{\sqrt{\theta}}\right)^2}{0.5}} = \frac{G}{\sqrt{\theta}}. \quad (14)$$

For the synaptic weights $g_{12} = 4.2$, $g_{23} = 12.0$, and $g_{31} = -8.6$, one obtains:

$$G = \sqrt{4.2^2 + 12^2 + (-8.6)^2} \approx 15.349.$$

Selecting $\theta = 0.5$, the ultimate bound is $b = G/\sqrt{\theta} = 21.703$.

By constructing the Lyapunov function and analyzing its derivative, the globally uniformly ultimate boundedness of the 3D het-CHNN is strictly proven by Theorem 4.18 of Khalil (2002), and the ultimate bound is determined jointly by the synaptic weights and the designed parameters θ.

Remark 1 The Lyapunov function $V(\boldsymbol{x})$ in Eq. (6) is a standard quadratic positive definite function, which can be expressed as the energy function of the 3D het-CHNN. From the above proof of boundedness, it can be seen that the energy function is helpful for understanding the boundedness of the 3D het-CHNN.

Remark 2 The energy function can illustrate the dissipative nature of the 3D het-CHNN. Observing Eq. (11), for large values of $\|\boldsymbol{x}\|$, the negative quadratic term plays a dominant role, causing $\dot{V}(\boldsymbol{x})$ to be less than 0. This indicates that the 3D het-CHNN is dissipative and that its energy will eventually decrease. Then, the system trajectory is bounded and will eventually become an attractor.

2.3 Equilibrium points with stability types

We set the equilibrium point of the 3D het-CHNN as $P = (X_1, X_2, X_3)$. Thus, we obtain:

$$\begin{cases} -X_1 + g_{12} \sin X_2 = 0, \\ -X_2 + g_{23} \cos X_3 = 0, \\ -X_3 + g_{31} \tanh X_1 = 0. \end{cases} \tag{15}$$

For the given synaptic weights, several non-zero equilibrium points exist, which are described as:

$$P = (X_1, X_2, g_{31} \tanh X_1), \tag{16}$$

where X_1 and X_2 are acquired through the non-zero intersections of the following two curves:

$$h_1(X_1, X_2) = -X_1 + g_{12} \sin X_2, \tag{17}$$

$$h_2(X_1, X_2) = -X_2 + g_{23} \cos(g_{31} \tanh X_1). \tag{18}$$

The Jacobian matrix at $P=(X_1, X_2, X_3)$ is obtained from Eq. (4) as:

$$\boldsymbol{J} = -\boldsymbol{I} + \boldsymbol{G}\boldsymbol{f}'(\boldsymbol{X}), \tag{19}$$

and the characteristic equation is thus

$$P(\lambda) = \det(\lambda \boldsymbol{I} - \boldsymbol{J}) = 0, \tag{20}$$

where λ is the characteristic root, $\boldsymbol{I} \in \mathbb{R}^{3\times3}$ represents the unit synaptic matrix, and $\boldsymbol{f}'(\boldsymbol{X}) = [\mathrm{sech}^2 X_1, \cos X_2, -\sin X_3]^{\mathrm{T}} \in \mathbb{R}^3$ represents the derivative of the synaptic matrix $\boldsymbol{f}(\boldsymbol{x})$ at $P=(X_1, X_2, X_3)$.

When the synaptic weights in Eq. (3) are fixed, the equilibrium points and corresponding eigenvalues can be solved numerically for the 3D het-CHNN. For fixed g_{12}=4.2, g_{23}=12.0, g_{31}=−8.6, and IS=(0.001, 0, 0), the equilibrium points with stability types are solved, and their projections on the X_1–X_2 plane are depicted in Fig. 3. The equilibrium points marked with blue, red, and green represent the index-1 unstable saddle focus (USF-1), the index-2 unstable saddle focus (USF-2), and the stable node focus (SNF), respectively. Thus, under this set of parameters, there are a total of 41 equilibrium points, including 20 USF-1 points, 20 USF-2 points, and an SNF point. Meanwhile, the phase orbit of the multi-scroll chaotic attractor in the x_1-x_2 plane is also plotted in Fig. 3.

It is well known that the USF-2 point is a necessary condition for a dynamical system to generate a self-excited chaotic attractor. Following the Shil'nikov theorem presented in Silva (1993), when a dynamical system adopts appropriate parameters, several USF-1 and USF-2 points will exist. In the neighborhoods of some of these equilibrium points, the dynamical system may produce corresponding attractor bonds and scrolls, thereby generating complex-structured multi-scroll chaotic attractors (Wang et al., 2019). Naturally, the greater the number of USF-1 and USF-2 points, the greater the number of attractor bonds and scrolls in the self-excited chaotic attractor.

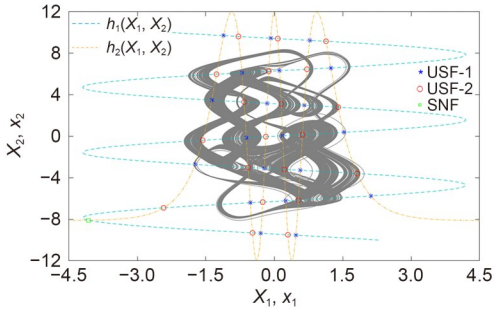

Fig. 3 Equilibrium points with stability types as well as the phase orbit of the multi-scroll chaotic attractor for fixed g_{12}=4.2, g_{23}=12.0, g_{31}=−8.6, and IS=(0.001, 0, 0)

For the 3D het-CHNN, it can be seen from Fig. 3 that the attractor scrolls overlap with a portion of the USF-2 points, indicating that the attractor scrolls are extremely correlated with the USF-2 points. Furthermore, due to the existence of an SNF point, any motion trajectory departing from the neighborhood of this SNF point gradually approaches a stable attraction domain, eventually forming a point attractor. Therefore, the motion trajectories starting from different initial states have at least two dynamical behaviors, namely, the multi-scroll chaotic attractor and the stable point; this demonstrates the emergence of bi-stability in the 3D het-CHNN.

3 Bifurcation dynamics and chaotic attractors

In this section, the bifurcation dynamics, multi-scroll chaotic attractor, and bi-stability are explored in the 3D het-CHNN.

3.1 Bifurcation dynamics

The synaptic weight g_{23} is considered the bifurcation parameter, which increases within the region [11, 16], and the other synaptic weights remain consistent with the synaptic weights in Fig. 2. Meanwhile, the initial states are determined as IS=(0.001, 0, 0). Note that the MATLAB RK-4 method with a step size of

0.01 and time range of [900, 1000] is used for the bifurcation plot, and Wolf's Jacobi algorithm with a step size of 1 and time end of 15000 is used for the LE spectra.

For g_{23} varying in the region [11, 16], the resulting bifurcation plot of the variable x_1 and the three LE spectra are shown in Figs. 4a and 4b, respectively. Clearly, the bifurcation behaviors observed in the bifurcation plot are consistent with those described by the LE spectra. Thus, various chaotic and periodic behaviors, as well as different types of chaotic and periodic bubble behaviors, are observable in the 3D het-CHNN.

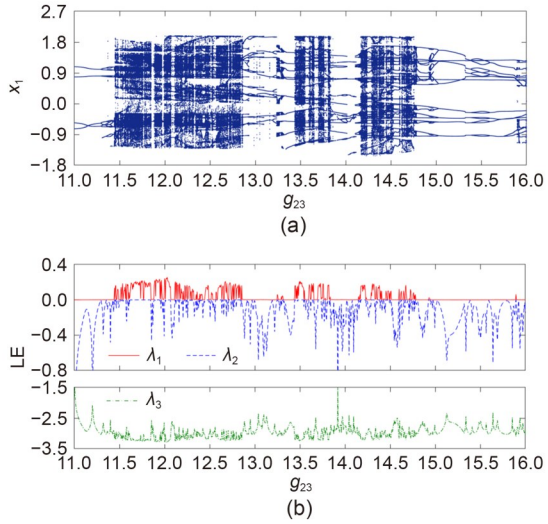

Fig. 4 Bifurcation behaviors when g_{23} is varied in the region [11, 16] for fixed g_{12}=4.2, g_{31}=−8.6, and IS=(0.001, 0, 0): (a) bifurcation plot of x_1; (b) three LE spectra

The synaptic weight-related bifurcation behaviors are illustrated by the results in Fig. 4. The chaotic orbits with one positive, one zero, and one negative LE are mainly located in the three regions of [11.44, 12.86], [13.44, 13.84], and [14.15, 14.79]. In these regions dominated by chaotic behaviors, there are numerous interspersed periodic windows, indicating the existence of complex evolving dynamics. The periodic orbits with one zero and two negative LEs are mainly distributed in the four regions of [11.00, 11.43], [12.87, 13.43], [13.85, 14.00], and [14.80, 16.00]. In these regions dominated by periodic behaviors, there are multiple chaotic and periodic bubbles, reflecting the emergence of complete and incomplete period-doubling bifurcation routes.

It is well known that by slowly changing bifurcation control parameters, periodic orbits can be generated and then disappear in reverse period-doubling bifurcation scenarios (Ding et al., 2024). This generation and destruction of periodic orbits is a phenomenon called anti-monotonicity, or bubble dynamics, and has been observed in many nonlinear dynamical systems (Liu et al., 2025).

The chaotic and periodic bubbles can be explained in detail by referring to the local bifurcation behaviors shown in Fig. 4. When g_{23} is varied in the regions of [13.28, 13.33] and [15.34, 15.64], the bifurcation plot of the variable x_1 and the first two LE spectra are shown in Figs. 5a and 5b, respectively. In the LE spectra, when λ_1=0 and λ_2 increases from a negative value and reaches zero, in the bifurcation plots, the trajectory splits from one into two or merges from two into one path, and a forward or reverse period-doubling bifurcation occurs at this time. Fig. 5a presents the forward and reverse complete period-doubling bifurcation scenarios, and Fig. 5b shows the forward and reverse incomplete period-doubling bifurcation scenarios, i.e., the anti-monotonicity phenomenon.

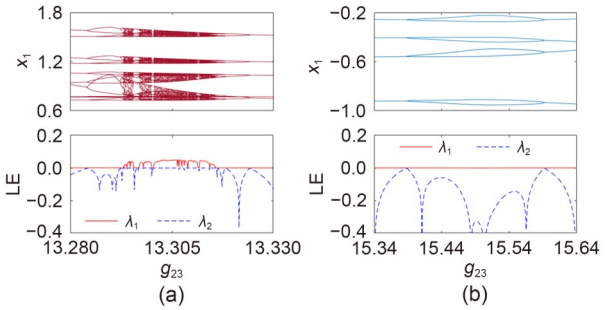

Fig. 5 Partial bifurcation behaviors described by the bifurcation plots and the first two LE spectra when g_{23} is varied in two different regions: (a) [13.28, 13.33]; (b) [15.34, 15.64]

3.2 Multi-scroll chaotic attractors

According to the bifurcation dynamics shown in Fig. 4, when g_{23}=12.0, a multi-scroll chaotic attractor is generated in the 3D het-CHNN; its phase orbit in the x_1–x_2 plane is depicted in Fig. 3. When the other two g_{23} values are selected, two multi-scroll chaotic attractors similar to the previous case are also produced in the 3D het-CHNN; their phase orbits in the x_1–x_2 plane are drawn in Fig. 6.

Specifically, for g_{23}=13.5, Fig. 6a presents the multi-scroll chaotic attractor with (λ_1, λ_2, λ_3)=(0.1809, −0.0001, −3.2108), while for g_{23}=14.6, Fig. 6b shows the multi-scroll chaotic attractor with (λ_1, λ_2, λ_3)=(0.1206,

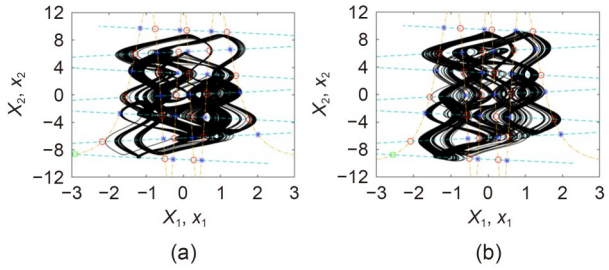

Fig. 6 Equilibrium points with stability types as well as the phase orbits of the multi-scroll chaotic attractor for fixed g_{12}=4.2, g_{31}=−8.6, and IS=(0.001, 0, 0) with two different g_{23} values: (a) g_{23}=13.5; (b) g_{23}=14.6

−0.0003, −3.1503). Meanwhile, for the two g_{23} values, the equilibrium points with stability types are solved for, and their projections on the X_1–X_2 plane are drawn in Figs. 6a and 6b, respectively. For these two different parameters, the positions of the equilibrium points change slightly, but their numbers and stability types remain unchanged.

3.3 Evolution of bi-stability

Because there is a stable point and a large number of unstable points in these equilibrium points, the 3D het-CHNN can show bi-stability with the coexistence of two attractor types. To this end, we utilize the variations in different stability distribution regions in the basins of attraction to characterize the evolution of bi-stability with the synaptic weights.

To explore the attraction domains of these two types of coexisting attractors, a basin of attraction is used to distinguish between the long-term dynamical behaviors of different initial states. By scanning each initial state on the $x_1(0)$-$x_2(0)$ plane with fixed $x_3(0)$=8.6, the basins of attraction (marked in different colors) are generated, and the results for three different g_{23} values are shown in Fig. 7. Note that the red and blue zones

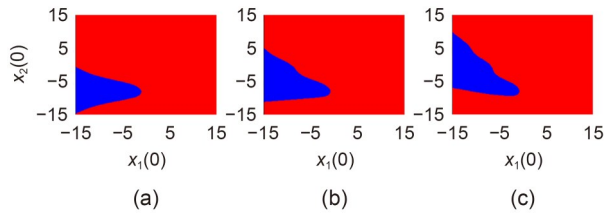

Fig. 7 Basins of attraction in the $x_1(0)$–$x_2(0)$ initial plane for IS=[$x_1(0)$, $x_2(0)$, 8.6] with different g_{23} values: (a) g_{23}=12.0; (b) g_{23}=13.5; (c) g_{23}=14.6. The multi-scroll chaotic attractor and the point attractor are marked with red and blue regions, respectively

represent the attraction domains of the two types of coexisting attractors.

As illustrated in Fig. 7, for these three different g_{23} values, two different attraction domains exist in these basins of attraction. Among them, the red zones for the multi-scroll chaotic attractors play a dominant role, and as the synaptic weight g_{23} increases, the blue zones for the stable point attractors gradually shift upward. However, on the whole, the coexistence of multi-scroll chaotic attractors and stable point attractors can still be maintained under different g_{23} values, indicating the existence of bi-stability in the 3D het-CHNN.

4 Analog circuit design and experiments

Using commercial electronic components, an analog circuit is developed to implement the 3D het-CHNN and validate the earlier numerical results.

4.1 Analog circuit design

Circuit implementation of HNNs is a crucial step in promoting their practical application. To this end, an analog circuit implementing the 3D het-CHNN is established, which is depicted in Fig. 8. It has three integration channels, each of which is followed by an activation function module. Three integration channels are respectively realized by operational amplifiers (U_1, U_4, and U_7), and they have the same time constant achieved

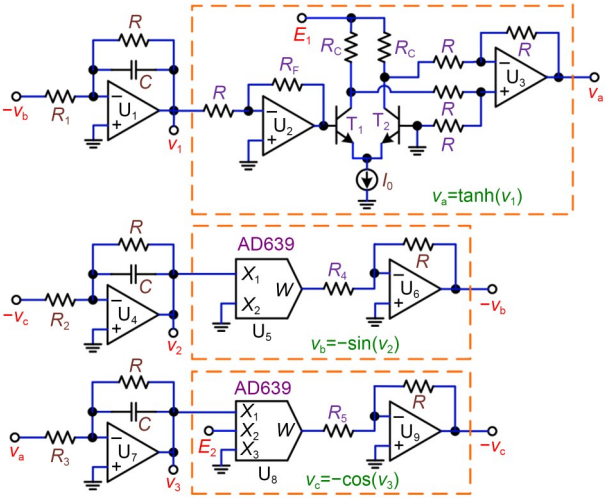

Fig. 8 Analog circuit for implementing the 3D het-CHNN, where two PN2222A transistors are used to implement the hyperbolic tangent module, and two AD639AD chips are used to implement the sine and cosine modules

by reference resistor R and reference capacitor C. Their input resistances are R_1, R_2, and R_3. The capacitor voltages v_1, v_2, and v_3 in the three integrator channels correspond to the state variables x_1, x_2, and x_3 in Eq. (4), respectively.

The hyperbolic tangent module in the first integration channel can be designed with reference to Bao et al. (2019), which consists of two operational amplifiers (U_2 and U_3), two PN2222A triode transistors (T_1 and T_2), a bias current source I_0, a bias voltage source E_1, two collector resistors with the same resistance R_C, a feedback resistor with resistance R_F, and five resistors with resistance R. Setting the element parameters to R=10 kΩ, R_C=1 kΩ, R_F=520 Ω, E_1=15 V, and I_0=1.19 mA, the hyperbolic tangent module model is thus v_a=tanh(v_1). The sine and cosine modules in the second and last integration channels are designed with two AD639AD trigonometric function converters (U_5 and U_8) and two inverters (U_6 and U_9) (Chen et al., 2019). Here, E_2 is the bias voltage of U_8, and R_4 and R_5 are the input resistances of U_6 and U_9, respectively. When X_1 is connected to v_2 and X_2 is grounded, W outputs a value of 10sin(v_2). By setting R_4=1 kΩ and R=10 kΩ, the sine module model is v_b=−(R_4/R)×10sin(v_2)=−sin(v_2). When X_1 is connected to v_3, X_2 is connected to E_2, and X_3 is grounded, W outputs a value of 5cos(v_3). By setting R_5=2 kΩ, R=10 kΩ, and E_2=5 V, the cosine module model is v_c=−(R_5/R)×5cos(v_3)=−cos(v_3).

Therefore, the circuit equations for implementing the circuit in Fig. 8 can be established as:

$$\begin{cases} \tau \dfrac{\mathrm{d}v_1}{\mathrm{d}t} = -v_1 + \dfrac{R}{R_1}\sin v_2, \\ \tau \dfrac{\mathrm{d}v_2}{\mathrm{d}t} = -v_2 + \dfrac{R}{R_2}\cos v_3, \\ \tau \dfrac{\mathrm{d}v_3}{\mathrm{d}t} = -v_3 - \dfrac{R}{R_3}\tanh v_1, \end{cases} \tag{21}$$

where τ is a time constant and τ=RC=10 kΩ×10 nF=100 μs. Using the synaptic weights shown in Fig. 2, the resistances are calculated as R_1=R/g_{12}=2.38 kΩ, R_2=R/g_{23}=833 Ω, and R_3=R/|g_{31}|=1.16 kΩ. Thus, the multi-scroll chaotic attractor in Fig. 2 can be realized by this circuit implementation of the 3D het-CHNN.

4.2 Analog circuit experiments

Based on the analog circuit designed in Fig. 8, a hardware circuit board can be fabricated, as shown in Fig. 9a. Here, TL082CP and AD711JN operational amplifier chips, AD639AD trigonometric function converter chips, chip capacitors, PN2222A triode transistors, precision potentiometers, and chip resistors, as well as +5 and ±15 V voltage supplies, are utilized. Meanwhile, a digital oscilloscope is used to capture the phase orbits in the X-Y mode. When tuning R_1=2.24 kΩ, R_2=790 Ω, and R_3=1.16 kΩ, the experimental hardware setup with the captured multi-scroll chaotic attractor is portrayed in Fig. 9b, thus verifying the numerical results shown in Fig. 2.

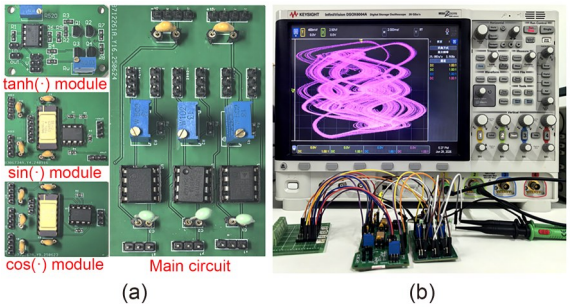

Fig. 9 Hardware setup: (a) hardware circuit board; (b) experimental platform

Considering the numerical results of Fig. 6, the multi-scroll chaotic attractors are obtained experimentally for two different resistances of R_2, and the resulting phase orbits on the v_1-v_2 phase planes are displayed in Fig. 10, where V/div refers to the voltage represented by each grid on the oscilloscope. Ignoring the errors in the resistance values, the experimental results demonstrate that the 3D het-CHNN can generate multi-scroll chaotic attractors, therefore verifying the numerical results in Fig. 6 and demonstrating the validity of the designed analog circuit.

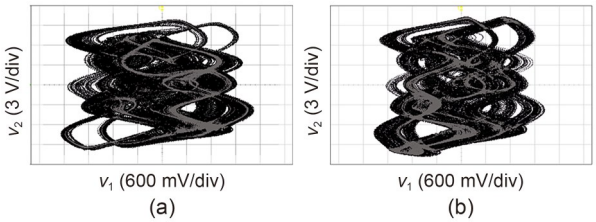

Fig. 10 Experimental phase orbits of the multi-scroll chaotic attractors following the results in Fig. 6: (a) R_2=698 Ω; (b) R_2=649 Ω

It should be noted that the proposed 3D het-CHNN is implemented based on the AD639AD trigonometric function converter chip, and the experimental

phase orbits of the multi-scroll chaotic attractors were successfully obtained from the hardware circuit board. Although analog circuit implementations using this function converter have been sporadically mentioned in the literature (e.g., Chen et al., 2020), only a few phase orbits of a dynamical system have been observed in such studies. Consequently, the present analog circuit has great practical significance, as it simplifies analog circuit implementation to facilitate potential applications of artificial intelligence (Zhang et al., 2025).

4.3 Error analysis of hardware experiments

In our hardware experiment, there was a discrepancy between the theoretical value and the actual value of the designed resistors used as synaptic weights. This is because there are inherent parasitic parameters in the PN2222A triode transistor, the AD639AD trigonometric converter, and other components, as well as external electromagnetic interference and instrument measurement errors. These result in inaccuracies in the hardware experimental measurements.

The absolute percentage error (E_{AP}) is used to evaluate the error between the theoretical and actual values of the designed resistors. It is expressed in the form of a ratio as:

$$E_{AP}=\left|\frac{R_{Actual}-R_{Theory}}{R_{Actual}}\right|\times 100\%, \tag{22}$$

where R_{Actual} represents the actual value and R_{Theory} represents the theoretical value of the resistor.

Table 1 E_{AP} values of R_{Theory} and R_{Actual} for different values of g_{12} and g_{23}

Weight	R_{Theory}	R_{Actual}	E_{AP}
g_{12}=4.2	$R_{1,Theory}$=2.38 kΩ	$R_{1,Actual}$=2.24 kΩ	6.25%
g_{23}=12.0	$R_{2,Theory}$=833 Ω	$R_{2,Actual}$=790 Ω	5.44%
g_{23}=13.5	$R_{2,Theory}$=741 Ω	$R_{2,Actual}$=698 Ω	6.16%
g_{23}=14.6	$R_{2,Theory}$=685 Ω	$R_{2,Actual}$=649 Ω	5.55%

For different values of g_{12} and g_{23}, the theoretical values of resistors R_1 and R_2 can be computed using $R_{1,Theory}=R/g_{12}$ and $R_{2,Theory}=R/g_{23}$, and the actual values of resistors R_1 and R_2 can be obtained through hardware experiments. The E_{AP} values are evaluated according to Eq. (22) and presented in Table 1. Accordingly, the maximum error between the theoretical and actual values is 6.25%, demonstrating that the hardware experiments are reliable.

5 Conclusions

In this study, we proposed a novel neural network architecture, the 3D het-CHNN. The hyperbolic tangent, sine, and cosine functions were used as the activation functions of the network's three neurons. Through theoretical proofs and numerical simulations, the boundedness, dynamical behaviors, and multi-scroll chaotic attractors of the network were presented and analyzed. Next, the 3D het-CHNN was implemented in an analog circuit, and hardware experiments were conducted with this circuit to confirm the previous numerical results. Notably, the proposed 3D het-CHNN successfully addresses the issue of the absence of chaos in a three-neuron CHNN. As far as the authors know, the 3D het-CHNN is the simplest three-neuron HNN that can generate multi-scroll chaotic attractors. Our findings may aid exploration of the mechanisms of neurodegenerative diseases, while the hardware circuit implementation of our network could be beneficial for various practical applications. Such aspects may be explored in future research.

Acknowledgments

This work is supported by the National Natural Science Foundation of China (Nos. 62571067 and 62201094), the Young Backbone Teachers Training Program of Henan Province (No. 2023GGJS142), the Key Research Program for Higher Education in Henan Province (No. 25A120009), and the 333 High-Level Talent Cultivation Project of Jiangsu Province, China.

Author contributions

Yunzhen ZHANG designed the research. Chunlong ZHOU processed the corresponding data. Yunzhen ZHANG and Han BAO wrote the first draft of the manuscript. Guangzhe ZHAO helped to organize the manuscript. Han BAO and Bocheng BAO revised and edited the final version.

Conflict of interest

Yunzhen ZHANG, Chunlong ZHOU, Han BAO, Guangzhe ZHAO, and Bocheng BAO declare that they have no conflict of interest.

References

Bao BC, Chen CJ, Bao H, et al., 2019. Dynamical effects of neuron activation gradient on Hopfield neural network: numerical analyses and hardware experiments. *International Journal of Bifurcation and Chaos*, 29(4):1930010. https://doi.org/10.1142/S0218127419300106

Bao BC, Tang HG, Su YH, et al., 2024. Two-dimensional discrete bi-neuron Hopfield neural network with polyhedral

hyperchaos. *IEEE Transactions on Circuits and Systems I: Regular Papers*, 71(12):5907-5918. https://doi.org/10.1109/TCSI.2024.3382259

Bao H, Chen ZG, Cai JM, et al., 2022. Memristive cyclic three-neuron-based neural network with chaos and global coexisting attractors. *Science China Technological Sciences*, 65(11):2582-2592. https://doi.org/10.1007/s11431-022-2144-x

Bao H, Chen ZG, Ma J, et al., 2024. Planar homogeneous coexisting hyperchaos in bi-memristor cyclic Hopfield neural network. *IEEE Transactions on Industrial Electronics*, 71(12):16398-16408. https://doi.org/10.1109/TIE.2024.3387058

Chen B, Xu Q, Chen M, et al., 2021. Initial-condition-switched boosting extreme multistability and mechanism analysis in a memcapacitive oscillator. *Frontiers of Information Technology & Electronic Engineering*, 22(11):1517-1531. https://doi.org/10.1631/FITEE.2000622

Chen CJ, Min FH, Cai JM, et al., 2024. Memristor synapse-driven simplified Hopfield neural network: hidden dynamics, attractor control, and circuit implementation. *IEEE Transactions on Circuits and Systems I: Regular Papers*, 71(5):2308-2319. https://doi.org/10.1109/TCSI.2024.3349451

Chen M, Ren X, Wu HG, et al., 2019. Periodically varied initial offset boosting behaviors in a memristive system with cosine memductance. *Frontiers of Information Technology & Electronic Engineering*, 20(12):1706-1716. https://doi.org/10.1631/FITEE.1900360

Chen M, Ren X, Wu HG, et al., 2020. Interpreting initial offset boosting via reconstitution in integral domain. *Chaos, Solitons & Fractals*, 131:109544. https://doi.org/10.1016/j.chaos.2019.109544

Danca MF, Kuznetsov N, 2017. Hidden chaotic sets in a Hopfield neural system. *Chaos, Solitons & Fractals*, 103:144-150. https://doi.org/10.1016/j.chaos.2017.06.002

Ding DW, Chen SQ, Zhang HW, et al., 2024. Firing pattern transition of fractional-order memristor-coupled Hindmarsh-Rose neurons model and its medical image encryption for region of interest. *Nonlinear Dynamics*, 112(12):10529-10554. https://doi.org/10.1007/s11071-024-09593-w

Gratwicke J, Jahanshahi M, Foltynie T, 2015. Parkinson's disease dementia: a neural networks perspective. *Brain*, 138(6):1454-1476. https://doi.org/10.1093/brain/awv104

Hopfield JJ, 1982. Neural networks and physical systems with emergent collective computational abilities. *Proceedings of the National Academy of Sciences of the United States of America*, 79(8):2554-2558. https://doi.org/10.1073/pnas.79.8.2554

Khalil HK, 2002. Nonlinear Systems. 3rd Edition. Prentice Hall, Upper Saddle River, USA.

Kobayashi M, 2020. Diagonal rotor Hopfield neural networks. *Neurocomputing*, 415:40-47. https://doi.org/10.1016/j.neucom.2020.07.041

Korn H, Faure P, 2003. Is there chaos in the brain? II. Experimental evidence and related models. *Comptes Rendus Biologies*, 326(9):787-840. https://doi.org/10.1016/j.crvi.2003.09.011

Lai Q, Wan ZQ, Kuate PDK, 2023. Generating grid multi-scroll attractors in memristive neural networks. *IEEE Transactions on Circuits and Systems I: Regular Papers*, 70(3):1324-1336. https://doi.org/10.1109/TCSI.2022.3228566

Lai Q, Yang L, Hu GW, et al., 2024. Constructing multiscroll memristive neural network with local activity memristor and application in image encryption. *IEEE Transactions on Cybernetics*, 54(7):4039-4048. https://doi.org/10.1109/TCYB.2024.3377011

Lei Z, Guo Q, Wang CN, et al., 2025. Continuous energy exchange between magnetic fields supporting memristive neuron firing. *Journal of Zhejiang University-SCIENCE A*, 26(8):755-770. https://doi.org/10.1631/jzus.A2500150

Li FY, Chen ZG, Zhang YZ, et al., 2024a. Cascade tri-neuron Hopfield neural network: dynamical analysis and analog circuit implementation. *AEÜ-International Journal of Electronics and Communications*, 174:155037. https://doi.org/10.1016/j.aeue.2023.155037

Li FY, Bai LF, Chen ZG, et al., 2024b. Scroll-growth and scroll-control attractors in memristive bi-neuron Hopfield neural network. *IEEE Transactions on Circuits and Systems II: Express Briefs*, 71(4):2354-2358. https://doi.org/10.1109/TCSII.2023.3331058

Li FY, Qin WS, Xi MQ, et al., 2025. Plane coexistence behaviors for Hopfield neural network with two-memristor-interconnected neurons. *Neural Networks*, 183:107049. https://doi.org/10.1016/j.neunet.2024.107049

Lin HR, Wang CH, Cui L, et al., 2022. Brain-like initial-boosted hyperchaos and application in biomedical image encryption. *IEEE Transactions on Industrial Informatics*, 18(12):8839-8850. https://doi.org/10.1109/TII.2022.3155599

Lin HR, Wang CH, Xu C, et al., 2023. A memristive synapse control method to generate diversified multistructure chaotic attractors. *IEEE Transactions on Computer-Aided Design of Integrated Circuits and Systems*, 42(3):942-955. https://doi.org/10.1109/TCAD.2022.3186516

Lin W, Chen GR, 2009. Large memory capacity in chaotic artificial neural networks: a view of the anti-integrable limit. *IEEE Transactions on Neural Networks*, 20(8):1340-1351. https://doi.org/10.1109/TNN.2009.2024148

Liu L, Huang Y, Chen ZG, et al., 2025. A dual-neuron memristive Hopfield neural network and its application in image encryption. *Nonlinear Dynamics*, 113(14):18705-18726. https://doi.org/10.1007/s11071-025-11141-z

Ma J, 2023. Biophysical neurons, energy, and synapse controllability: a review. *Journal of Zhejiang University-SCIENCE A*, 24(2):109-129. https://doi.org/10.1631/jzus.A2200469

McFarlan AR, Chou CYC, Watanabe A, et al., 2023. The plasticitome of cortical interneurons. *Nature Reviews Neuroscience*, 24(2):80-97. https://doi.org/10.1038/s41583-022-00663-9

Njitacke ZT, Isaac SD, Nestor T, et al., 2021. Window of

multistability and its control in a simple 3D Hopfield neural network: application to biomedical image encryption. *Neural Computing and Applications*, 33(12):6733-6752. https://doi.org/10.1007/s00521-020-05451-z

Prescott SL, Liberles SD, 2022. Internal senses of the vagus nerve. *Neuron*, 110(4):579-599. https://doi.org/10.1016/j.neuron.2021.12.020

Rech PC, 2015. Period-adding and spiral organization of the periodicity in a Hopfield neural network. *International Journal of Machine Learning and Cybernetics*, 6(1):1-6. https://doi.org/10.1007/s13042-013-0222-0

Silva CP, 1993. Shil'nikov's theorem-a tutorial. *IEEE Transactions on Circuits and Systems I: Fundamental Theory and Applications*, 40(10):675-682. https://doi.org/10.1109/81.246142

Tang D, Wang CH, Lin HR, et al., 2024. Dynamics analysis and hardware implementation of multi-scroll hyperchaotic hidden attractors based on locally active memristive Hopfield neural network. *Nonlinear Dynamics*, 112(2):1511-1527. https://doi.org/10.1007/s11071-023-09128-9

Wan QZ, Li F, Chen SM, et al., 2023. Symmetric multi-scroll attractors in magnetized Hopfield neural network under pulse controlled memristor and pulse current stimulation. *Chaos, Solitons & Fractals*, 169:113259. https://doi.org/10.1016/j.chaos.2023.113259

Wang CH, Liang JH, Deng QL, 2024. Dynamics of heterogeneous Hopfield neural network with adaptive activation function based on memristor. *Neural Networks*, 178:106408. https://doi.org/10.1016/j.neunet.2024.106408

Wang N, Li CQ, Bao H, et al., 2019. Generating multi-scroll Chua's attractors via simplified piecewise-linear Chua's diode. *IEEE Transactions on Circuits and Systems I: Regular Papers*, 66(12):4767-4779. https://doi.org/10.1109/TCSI.2019.2933365

Xie Y, Yao Z, Ma J, 2022. Phase synchronization and energy balance between neurons. *Frontiers of Information Technology & Electronic Engineering*, 23(9):1407-1420. https://doi.org/10.1631/FITEE.2100563

Xu SC, Wang XY, Ye XL, 2022. A new fractional-order chaos system of Hopfield neural network and its application in image encryption. *Chaos, Solitons & Fractals*, 157:111889. https://doi.org/10.1016/j.chaos.2022.111889

Yang XS, 2008. 3-D cellular neural networks with cyclic connections cannot exhibit chaos. *International Journal of Bifurcation and Chaos*, 18(4):1227-1230. https://doi.org/10.1142/S0218127408020951

Yu F, Shen H, Yu QL, et al., 2023. Privacy protection of medical data based on multi-scroll memristive Hopfield neural network. *IEEE Transactions on Network Science and Engineering*, 10(2):845-858. https://doi.org/10.1109/TNSE.2022.3223930

Yu F, Lin Y, Yao W, et al., 2025a. Multiscroll Hopfield neural network with extreme multistability and its application in video encryption for IIoT. *Neural Networks*, 182:106904. https://doi.org/10.1016/j.neunet.2024.106904

Yu F, Su D, He SQ, et al., 2025b. Resonant tunneling diode cellular neural network with memristor coupling and its application in police forensic digital image protection. *Chinese Physics B*, 34(5):050502. https://doi.org/10.1088/1674-1056/adb8bb

Zhang M, Eichhorn SW, Zingg B, et al., 2021. Spatially resolved cell atlas of the mouse primary motor cortex by MERFISH. *Nature*, 598(7879):137-143. https://doi.org/10.1038/s41586-021-03705-x

Zhang S, Chen CJ, Zhang YZ, et al., 2025. Multidirectional multidouble-scroll Hopfield neural network with application to image encryption. *IEEE Transactions on Systems, Man, and Cybernetics: Systems*, 55(1):735-746. https://doi.org/10.1109/TSMC.2024.3489226

Zhou CL, Bao H, Zhang YZ, et al., 2026. Memory capacity expansion in a sine activated Hopfield neural network. *Chaos, Solitons & Fractals*, 205:117843. https://doi.org/10.1016/j.chaos.2025.117843